Int. J. Electrochem. Sci., 14 **(2019)** 4338 – 4349, doi: 10.20964/2019.05.30

International Journal of
ELECTROCHEMICAL
SCIENCE
www.electrochemsci.org

Effect of Current Density on Characteristics of 2024 Aluminum Alloy Microarc Oxidation Coatings with Titanium Dioxide Particles

Ping Wang[1,2], Wei Xiao Wei[1,], Jun Pu[2], Xiao Long Zhou[2], Wen Jie Cao[2], You Tao Xiao[2], Ze Yu Gong[2], Jie Hu[2]*

[1] The Postdoctoral Station at Xihua University Based on Collaboration Innovation Center of Sichuan Automotive Key Parts, School of Materials Science and Engineering, Xihua University, Chengdu, 610039, China
[2] School of Materials Science and Engineering, Southwest Petroleum University, Chengdu, 610500, China
[*]E-mail: weixiaowei90@yeah.net

Received: 4 January 2019 / *Accepted:* 23 February 2019 / *Published:* 10 April 2019

Ceramic coatings were deposited on a 2024 aluminum alloy by microarc oxidation (MAO) in a silicate electrolyte system containing 2 g/L nano-TiO_2 particles at different current densities (1, 2.5, 5, 7.5 and 10 A/dm^2). The oxidation voltage, surface and cross-section morphologies and corrosion resistance of the coatings were studied. The results indicated that the voltage increased and facilitated the growth rate of MAO coatings so that the coatings thickened as the current density increased. The size of the micropores on the coating surface first increased and then decreased, and the shape changed from a strip-shaped hole to a round hole. The microhardness and the coating adhesive strength improved with increasing current density, whereas the corrosion resistance of the coatings decreased first and then increased. The coatings were mainly composed of γ-Al_2O_3, SiO_2, mullite, TiO_2 and a small amount of α-Al_2O_3. As a whole, the discharge energy increased with increasing current density, and the microarc oxidation reactions became more intense, which contributed to the variation in the characteristics of the coatings.

Keywords: Microarc oxidation; Current density; 2024 aluminum alloy; Nano-TiO_2 particles

1. INTRODUCTION

Due to their high strength, favorable heat resistance and good processing performance, 2024 aluminum alloys are widely used in aerospace engineering applications. Nevertheless, their corrosion

resistance is poor [1], which severely limits their wider application. Surface treatment of 2024 aluminum alloys is imperative to improve their corrosion resistance and functionality. In recent years, new surface treatment technologies, such as ion implantation [2], chemical vapor deposition (CVD) [3], and laser surface treatment [4], have not been widely used owing to their complex operation and low production efficiency, for example. Microarc oxidation (MAO) is a new technology with wide application prospects that has attracted attention because of its simple operation, low cost and environmental friendliness [5-8]. Ceramic coatings have been produced on the surfaces of valve metals (such as magnesium, aluminum and titanium and their alloys) with different electrolytes, substrate materials and process parameters (such as current density, voltage, pulse frequency and duty cycle) [9-13], and these parameters have been shown to have a great influence on the properties of the coatings. It was found that adding nano-TiO_2 particles in the electrolyte improved the corrosion resistance [14-16] compared to coatings without the nano-TiO_2 particles. Therefore, MAO treatment that includes doping with nano-TiO_2 particles is likely to improve the performance of a 2024 aluminum alloy. Moreover, it is necessary to consider the effect of the current density on the MAO coatings containing nano-TiO_2 particles because the current density is an important factor to influence the performance ofr the coatings.

In this study, MAO coatings were produced on 2024 aluminum alloys at 1, 2.5, 5, 7.5 and 10 A/dm^2 separately with 2 g/L nano-TiO_2 particles in a Na_2SiO_3 electrolyte system. The influence of different current densities on the voltage, surface and cross-section morphologies, phase composition, coating adhesive strength, thermal shock resistance and corrosion resistance of the MAO coatings was investigated.

2. EXPERIMENTAL

Parallelepiped samples with dimensions of 15 mm×15 mm×2 mm were used as substrate materials and were cut from 2024 aluminum alloy plates (with a chemical composition in wt% of 3.8%-4.9% Cu, 0.3%-0.9% Mn, 1.2%-1.8% Mg, 0.1% Cr, 0.25% Zn, 0.5% Si, 0.5% Fe, 0.15% Ti and Al balance), polished and degreased before the MAO process. The base electrolyte was prepared from distilled water containing Na_2SiO_3 (18 g/L), NaOH (1 g/L) and $C_3H_8O_3$ (3 ml/L). The nano-TiO_2 particles were stirred continuously during the entire experiment to maintain a uniform dispersion. The MAO process was conducted using pulsed electrical power to provide a positive pulse current. The MAO coatings were obtained with peak current densities of 1, 2.5, 5, 7.5 and 10 A/dm^2 for 30 min with a duty cycle of 60%. The temperature of the electrolyte was kept below 30°C by a circulating cooling system. After the MAO process, the specimens were immersed in hot water at 95°C for 10 min and then dried by an electric hair dryer.

The surface and cross-sectional morphologies of MAO coatings were observed by a Scanning Electron Microscope (SEM, ZEISS EVO MA15) equipped with an Energy Dispersive Spectrometer (EDS, OXFORD 20). The phase composition of coatings was investigated by X-ray Diffraction (XRD, DX-2700B). The data were acquired over a 2θ scattering angle from 10° to 80°. The scratch tests were carried out to evaluate the adhesion between coatings and substrate by multifunctional surface

performance tester (MFT-4000) with the automatic loading from 0 to 20 N and loading rate was 10N/min. The thermal shock tests of the coatings were conducted by chamber electric furnace (SX-10-12) at 500°C for 10 min and then cooled in 25°C water for 50 cycles. Meanwhile, the microhardness, thickness and polarization curves of the coatings were investigated by Digital microhardness tester (HVS-1000) at 1 N for 15 s, Digital Thickness Gauges (TT230) and Electrochemical Workstation (PGSTAT302N, Switzerland), respectively. The scanning rate of the polarization curve was 1.5 $mV \cdot s^{-1}$ with a potential range from -1.0 V to -0.4 V.

3. RESULTS AND DISCUSSION

3.1. Voltage-time curves

Fig.1 shows the voltage transient during the MAO process at the current densities of 1, 2.5, 5, 7.5 and 10 A/dm^2 for 30 min. Three different stages in the voltage-time response can be observed clearly in Fig. 1, which agrees with the previous report about the MAO process [17]. At the initial anodic oxidation stage, the voltage values increased linearly to attain dielectric breakdown, consistent with the original formation mechanism of the MAO coatings [18]. In the second stage, known as spark anodization, the voltage began to exceed the breakdown voltage, and the phenomenon of electric arc discharge occurred. In the third stage, known as microarc oxidation, the voltage increased slowly and smoothly. The oxidation voltage gradually increased with increasing current density, while the added value of the oxidation voltage decreased. The increased oxidation voltage was induced by the increase in electric energy due to the ascending current density.

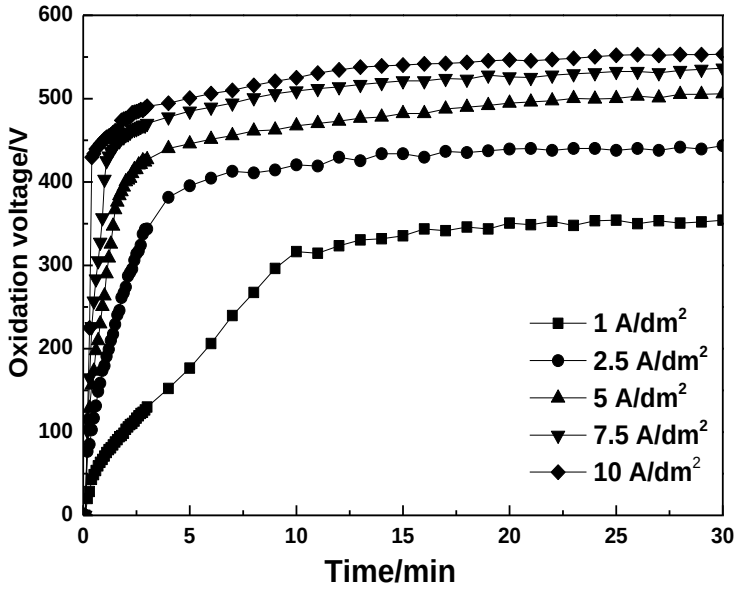

Figure 1. Oxidation voltage-time curves of the samples prepared using different current densities.

3.2. The surface morphologies and element content of coatings

The surface morphologies and elements present in the MAO coatings formed under different current densities are shown in Fig. 2(a)-(e). All the coatings revealed a characteristic feature of MAO coatings, which is the presence of many micropores surrounded by an accumulation of erupted and solidified sintered discs, where the discharge pores on the sintered discs increased as the current density increased, as shown in Fig. 2 (e). It is clear that at the relatively low current density of $1A/dm^2$, the surface morphologies were smooth and compact due to the weak intensity of discharge sparks. As the rising of current density from 2.5 A/dm^2 to 10 A/dm^2, the size of the pores on the coating surface first increased and then decreased, and the shape changed from strip-shaped holes to round holes. As mentioned above, the raise of oxidation voltage signified the ascending of electric energy, which gave rise to strong discharge sparks and dielectric breakdown on the coating surface. Moreover, the temperature of micro-areas boosted to 10^3-10^4 K [19] during the spark discharge process, which was sufficient to melt the micro-areas and form large-size pores, in accordance with the research results by Xiang [20]. Nevertheless after the addition of nano-TiO_2 particles, the molten oxidation coatings were impacted by the nano-TiO_2 during the cooling and solidification process. The nano-TiO_2 particles attached to the surface of coatings, which facilitated impurity nucleation in the molten oxidation coatings [21]. Furthermore, the addition of nano-TiO_2 particles could restrain the large spark discharge to form small discharge channels [15]. Hence, the combined effects of the two led to a decrease in pore size.

At the same time, it can be observed that the contents of Ti and O increased, whereas the content of Al decreased, and that of Si increased first and then decreased, as shown in Fig. 2. It is obvious that the Si and Ti elements came from the electrolyte, demonstrating that nano-TiO_2 particles were involved in the formation of the MAO coatings. With the increase of current density, the oxidation reactions were more intense and the thickness of coatings grew gradually, so the elements in the electrolyte solution (including the O produced by electrolysis) entered the coatings readily; it was more difficult for Al to travel to the coating surface because of the thickening of the coatings. Therefore, the contents of Ti, O and Si showed an upward trend, but the content of Al ultimately decreased as the current density increased. The main reactions during the MAO process are as follows [16, 22]:

$$2Al^{3+} + 3SiO_3^{2-} \rightarrow 3SiO_2 + Al_2O_3 \quad (1)$$

$$SiO_3^{2-} + Al_2O_3 + H_2O \rightarrow H_2SiO_3 + 2AlO_2^- \quad (2)$$

$$2Al_2O_3 + 3H_2SiO_3 \rightarrow 3Al_2O_3 \cdot 2SiO_2 + 3H_2O \quad (3)$$

$$H_2SiO_3 \rightarrow H_2O + SiO_2 \quad (4)$$

$$TiO_2(particle) \xrightarrow{micro-arc} TiO_2(melt) \xrightarrow{cooling} TiO_2(coating) \quad (5)$$

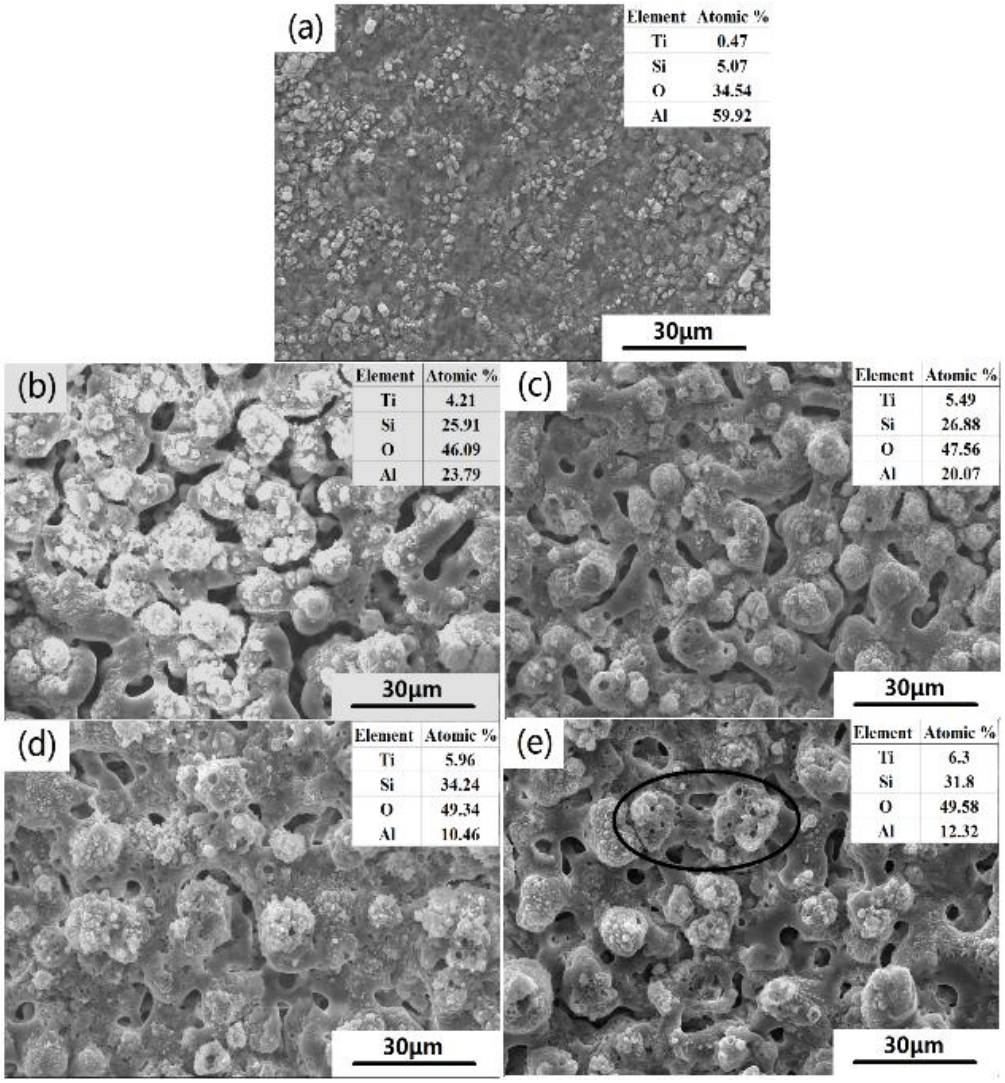

Figure 2. Surface morphologies and elemental contents of MAO coatings prepared using different current densities: (a) 1 A/dm^2, (b) 2.5 A/dm^2, (c) 5 A/dm^2, (d) 7.5 A/dm^2 and (e) 10 A/dm^2.

3.3. The cross-sectional morphologies of coatings

The cross-section microstructure of MAO coatings prepared using different current densities is shown in Fig. 3. It is apparent that the thickness of the coatings revealed a rising trend as the current density increased, which is in accordance with the thickness test in Fig. 4. Higher electric energy could be obtained due to a higher current density, and the discharge breakdown was strong, which facilitated the formation of the oxidation coatings. It is well known that the higher the current density is, the faster the growth rate [23-24]. Furthermore, the cross-section morphologies of the coatings were smooth and compact first and then gradually became porous due to the increase of the current density, which was consistent with the surface morphologies. On the other hand, the EDS results showed that the intensity of Ti increased with increasing current density. A mass of Ti was found near the outer surface of the coatings, indicating that Ti came from the electrolyte and ultimately entered into the coatings.

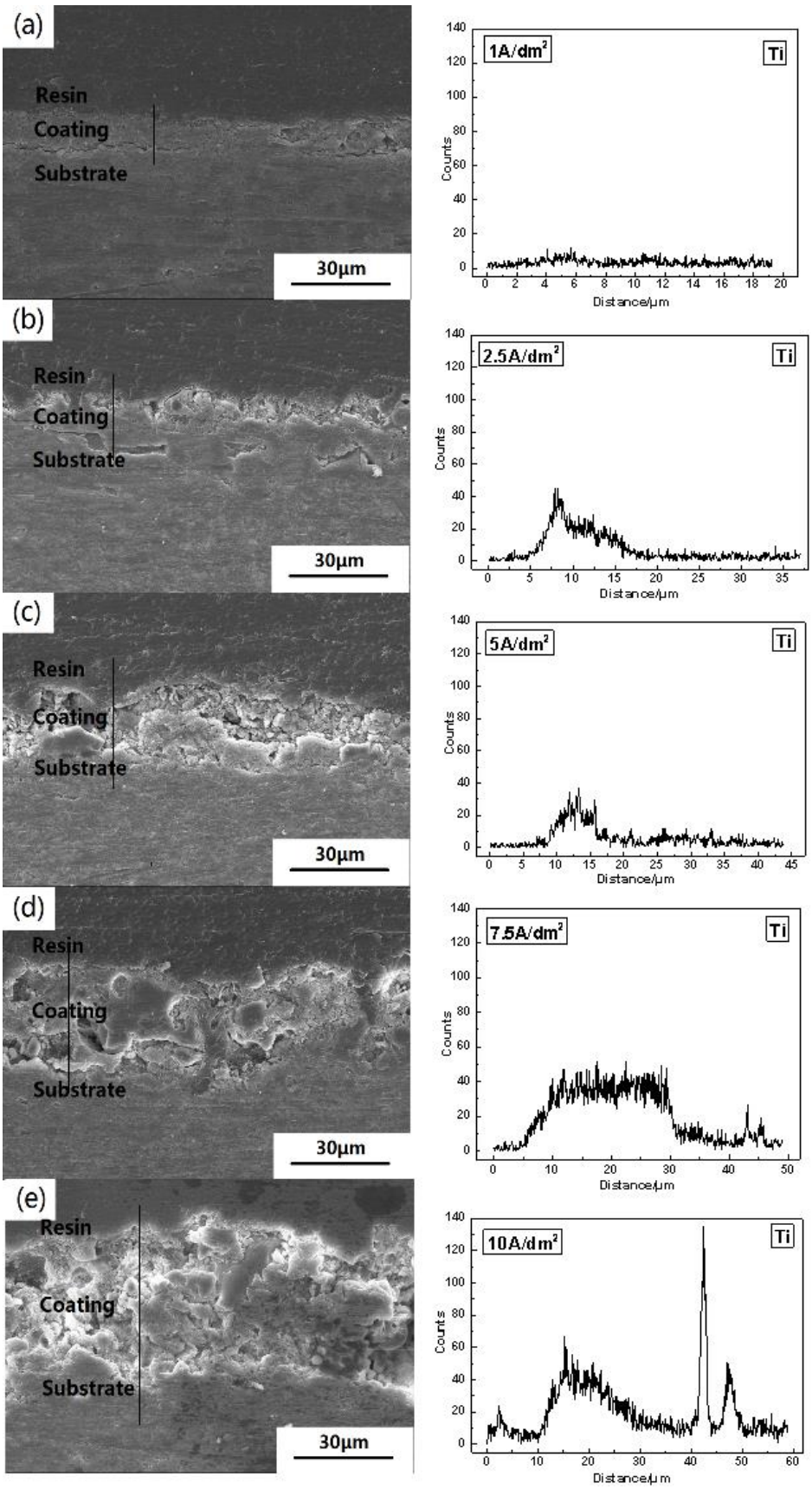

Figure 3. Cross-section images and Ti distribution of the samples prepared using different current densities: (a) 1 A/dm^2, (b) 2.5 A/dm^2, (c) 5 A/dm^2, (d) 7.5 A/dm^2 and (e) 10 A/dm^2.

3.4. The microhardness and thickness of coatings

The microhardness and thickness test results are depicted in Fig. 4. Both the microhardness and thickness of the coatings increased linearly with increasing current density. On the one hand, the rising current density promoted the increase in electric energy, and the higher electric energy was beneficial to the transformation from amorphous Al_2O_3 to γ-Al_2O_3, eventually turning it into a high-hardness α-Al_2O_3 due to the high-temperature electric arc. On the other hand, nano-TiO_2 particles attached to the interstices of the porous layer on the surface of coatings, which reduced the porosity and strengthened the compactness of the coatings, leading to an improvement in the microhardness. The increased thickness of the coatings demonstrated that increasing the current density was beneficial to the growth of the coatings.

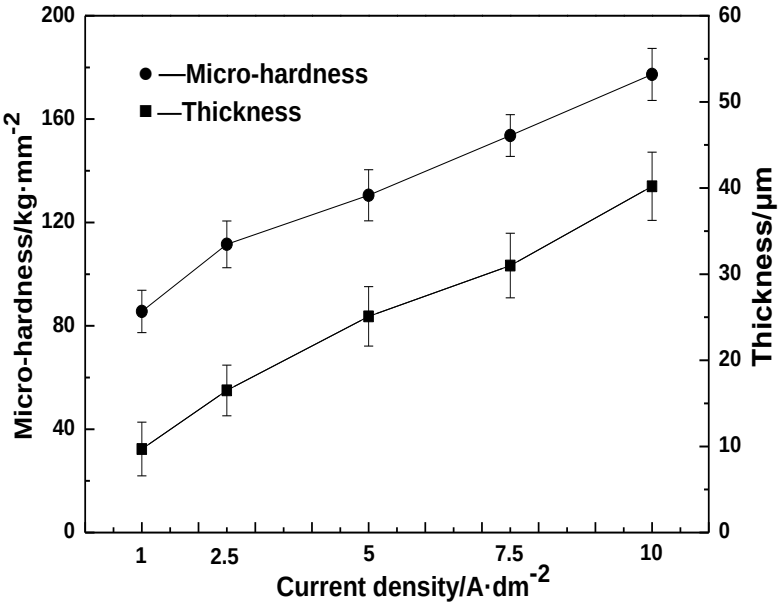

Figure 4. The microhardness and thickness of the samples prepared using different current densities.

3.5. The phase composition of coatings

Fig. 5 shows the X-ray diffraction patterns of the coatings prepared using different current densities. The result indicates that the coatings consist of γ-Al_2O_3, SiO_2, mullite, TiO_2 and a small amount of α-Al_2O_3. The peak intensities of TiO_2 and SiO_2 increased slightly when the current density increased. As discussed above, the high electric energy accelerated the transformation from amorphous Al_2O_3 to γ-Al_2O_3 and even α-Al_2O_3 eventually due to the rising current density. The detection of TiO_2 and SiO_2 showed that nano-TiO_2 particles and SiO_3^{2-} were involved in the formation of oxidation coatings, as presented in the chemical equations (1)-(5). The results were in agreement with the surface morphologies and EDS results.

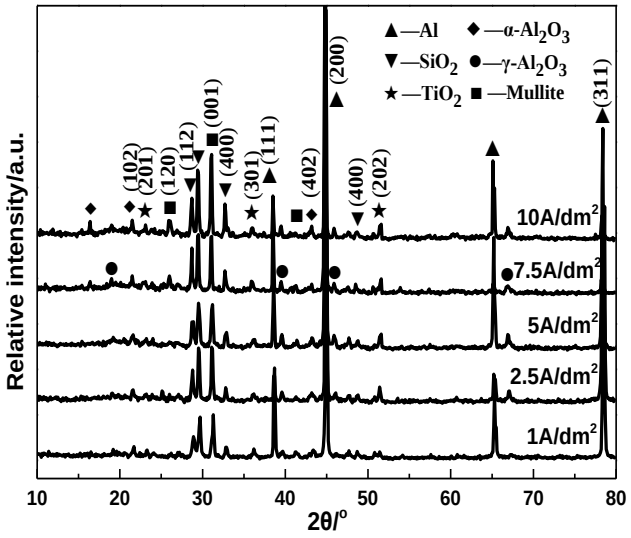

Figure 5. XRD spectra of the samples prepared using different current densities.

3.6. The coating adhesive strength

As shown in Fig. 6, it is clear that the critical load increased gradually by the scratch test results. The value of the critical load was used to estimate the adhesion strength between the coatings and substrates, and it varied in direct proportion to the adhesion [22]. Consequently, the adhesive strength between the coatings and substrates strengthened with the increasing current density. At high current densities, more γ-Al_2O_3 and α-Al_2O_3 phases were formed, which improved the adhesive strength between the coatings and substrates. Liu [25] found that with an increase of current density, strong diffusion occurred at the interface between the substrates and the coatings, resulting in the coatings being combined with the substrates via zigzag metallurgical bonding; thus, the coatings had good adhesion strength. Furthermore, the formation of round holes compared with strip-shaped holes was advantageous for the stress release. On the other hand, the thickened coatings were beneficial to the enhancement of adhesive strength between the coatings and substrates.

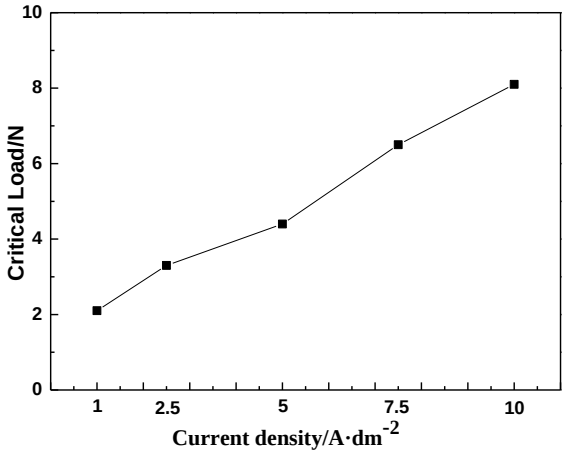

Figure 6. Variation in the critical load of the samples prepared using different current densities.

3.7. The thermal shock resistance of coatings

Figures 7(a) and (b) exhibit the surface morphologies of the thermal shock tests at 5 A/dm^2. The thermal shock resistance reflects not only the antistripping capacity of the surface coatings with the alternative variation in temperature during the process, but also the bonding strength between the coating and the substrate, which is a key comprehensive performance index to evaluate the stability of coatings [26]. From Fig. 7 (a), it is obvious that no peeling appeared on the coating surface of the samples at 500°C for 50 cycles, but there were some visible cracks locally on the coating surface, as shown in Fig. 7 (b). There was a large difference in the thermal expansion coefficient between the coating and the substrate; moreover, there was a large internal stress during the cooling process, leading to the propagation of microcracks on the coatings. At the same time, the moderate pores on the coatings could effectively reduce the centralization of internal stress and restrain the nucleation and expansion of thermal shock cracks, which is beneficial to improve the thermal shock resistance [27].

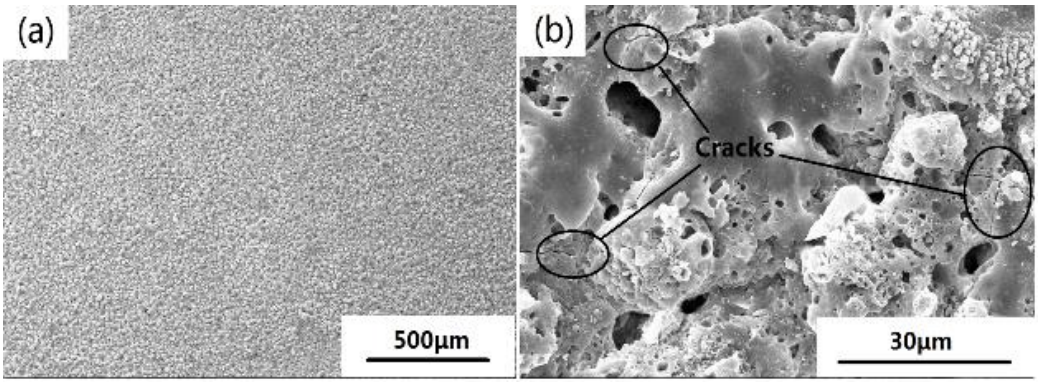

Figure 7. Surface morphologies of the coating at 5 A/dm^2 after the thermal shock tests: (a) 100 times and (b) 3000 times.

3.8. The corrosion resistance of coatings

Fig. 8 shows the potentiodynamic polarization curves in a 3.5 wt% NaCl solution of the MAO coatings prepared using different current densities. Table 1 represents the fitting results of the polarization curves. As a rule, in polarization curves, a higher corrosion potential and lower corrosion current density indicate a lower corrosion rate and better anti-corrosion behavior. From Fig. 8 and Table 1, the corrosion rate of the coatings first increased and then decreased gradually, which demonstrated that the corrosion resistance of the coatings first decreased and then finally increased. The inchoate reduction in corrosion resistance was ascribed to the increase in the number and size of microholes on the coating surface. The porosity of the coatings facilitated more Cl^- anions entering into the MAO coatings, which resulted in a decrease in the corrosion resistance of the coatings. As the current density increased, the size of the microhole on the coating surface decreased; at the same time, the thickening of the coatings restrained the approach of eroding Cl^- anions to the substrate and enhanced the corrosion resistance of the coatings. Yang [28] found that magnesium samples treated by MAO also had a good corrosion protective property compared with the magnesium substrate, and the

coating prepared at 5 A/dm^2 showed the best corrosion resistance due to the compact structure at the current density of 5 A/dm^2.

.

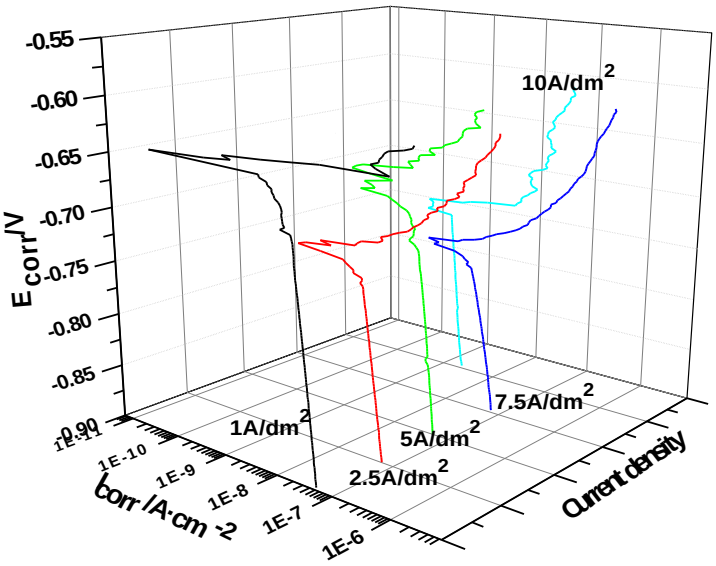

Figure 8. Polarization curves of the samples prepared using different current densities.

Table 1. Results of polarization curve analysis

Current density/ (A/dm^2)	E_{corr}/V	I_{corr}/(A/cm^2)	Corrosion rate/(mm/a)
1	-0.63	7.48×10^{-8}	9.15×10^{-3}
2.5	-0.72	1.11×10^{-7}	1.36×10^{-2}
5	-0.65	8.32×10^{-8}	1.02×10^{-2}
7.5	-0.75	1.25×10^{-7}	1.53×10^{-3}
10	-0.74	5.25×10^{-9}	6.43×10^{-4}

4. CONCLUSIONS

MAO coatings were fabricated on 2024 aluminum alloy substrates by MAO with the addition of 2 g/L nano-TiO_2 particles. The nano-TiO_2 particles were successfully incorporated into MAO coatings in silicate electrolyte, which was confirmed by EDS and XRD analysis. The variation of current density considerably affected surface morphologies, coating thickness, micro-hardness, phase compositions, adhesive strength and corrosion resistance of MAO coatings. As the current density increased, the higher energy enhanced the oxidation voltage and promoted the growth rate of the coatings, increasing the coating thickness. The size of microholes on the coating surface increased first due to the intense microarc oxidation reactions under higher electric energy, whereas the addition of

nano-TiO_2 particles restrained the large spark discharge, and many small discharge channels were formed, ultimately leading to a reduction in the micropore sizes. The MAO coatings mainly consisted of γ-Al_2O_3, SiO_2, mullite, TiO_2 and a small amount of α-Al_2O_3. The microhardness and the coating adhesive strength increased with increasing current density, whereas the corrosion resistance of the coatings decreased first and then increased..

ACKNOWLEDGEMENT
This work was supported by the Chunhui Project of Education Ministry of China (No. Z2011074); the Support Program of Wear and Friction Surface Engineering Research Center of Sichuan Provincial Education Department.

CONFLICTS OF INTEREST
The authors declare that there are no conflicts of interest regarding the publication of this paper.

References

1. J. Wang and R.G. Guo, *Mater. Prot.,* 47(2014)1.
2. L.X. Yuan, D.W. Tang, S.L. Zou, J. Liu and P.X. Li, *Surf. Technol.*, 44(2015)43.
3. X.K. Li, L. Chen, H.Z. Cai, Q.L. Wei and C.Y. Hu, *Rare Met. Mat. Eng.*, 39(2010)438.
4. D. Bhaduri, P. Penchev, A. Batal, S. Dimov, S.S. Leung, S. Sten, U. Harrysson, Z.X. Zhang and H.S. Dong, *Appl. Surf. Sci.*, 405(2017)29.
5. W.B. Xue, X.L. Shi, M. Hua and Y.L. Li, *Appl. Surf. Sci.,* 253(2007)6118.
6. Y.N. Xue, X. Pang, B.L. Jiang and H. Jahed, *Int. J. Electrochem. Sci.,* 13(2018)7265.
7. P. Wang, T. Wu, H. Peng and X.Y. Guo, *Mater. Lett.,* 170(2016)171.
8. F. Chen, H. Zhou, B. Yao, Z. Qin and Q.F. Zhang, *Surf. Coat. Technol.,* 201(2007)4905.
9. Y.Y. Fang, X.H. Tu, C.P. Miao, Y.L. Xu, W. Xie, F.D. Chen, Y. Zhang and J.Y. Li, *Int. J. Electrochem. Sci.,* 12(2017)11473.
10. C.Z. Wang, D. Zhang and Y.F. Jiang, *Appl. Surf. Sci.,* 253(2006)674.
11. T.B. Wei, F.Y. Yan and J. Tian, *J. Alloys Compd.,* 389(2005)169.
12. C.E. Barchiche, E. Rocca and J. Hazan, *Surf. Coat. Technol.,* 202(2008)4145.
13. W.B. Xue, Z.W. Deng, R.Y. Chen, T.H. Zhang and H. Ma, *J. Mater. Sci.,* 36(2001)2615.
14. Y.L. Song and Y.H. Liu, *Mater. Corros.,* 63(2012)813.
15. W. Leon, K. Youngmi, Y. Yeoheung and S. Jagannathan, *J. Nanomater.,* 11(2013)1.
16. H.X. Li, R.G. Song and Z.G. Ji, *Trans. Nonferrous. Met. Soc. China*, 23(2013)406.
17. Y.L. Cheng, F. Wu, J.L. Dong, X.Q. Wu, Z.G. Xue, E. Matykina, P. Skeldon and G.E. Thompson, *Electrochim. Acta*, 85(2012)25.
18. R.O. Hussein, X. Nie and D.O. Northwood, *Electrochim. Acta*, 112(2013)111.
19. V. Shoaei Rad, M.R. Bayati, H.R. Zargar, J. Javadpour and F. Golestani Fard, *Mater. Res. Bull.,* 47(2012)1494.
20. N. Xiang, R.G. Song, J.J. Zhuang, R.X. Song, X.Y. Lu and X.P. Su, *Trans. Nonferrous. Met. Soc. China*, 26(2016)806.
21. P. Wang, T. Wu, J. Li, X.H. Jia, C.L. Gong and X.Y. Guo, *Rare Met. Mat. Eng.*, 46(2017)479.
22. P. Wang, T. Wu, Y.T. Xiao, J. Pu, X.Y. Guo, J. Huang and C.L. Xiang, *J. Mater. Eng. Perform.*, 25(2016)3972.
23. Y. Yang and H. Wu, *J. Mater. Sci. Technol.*, 28(2012)321.
24. P. Wang, X.Y. Guo, C.H. Wang, J. Yang, F. Yi and Z.X. Xu, *Rare Met. Mat. Eng.*, 41(2012)174.

25. Z.D. Liu, Z.Q. Xiang, Z.Y. Zhang, M.J. Sun and H. Fu, *Light Metal*, 1(2008)48.
26. W.Q. Weng, J.M. Hao, Y.N. Chen, H. Chen, *China Ceram.,* 51(2015)34.
27. Q. Qu, Z.Y. Cai, W.B. Han, *Aerosp. Mater. Technol.,* 2(2010)28.
28. Y. Yang and H. Wu, *Trans. Nonferrous. Met. Soc. China*, 20(2010)s688.